RESEARCH ARTICLE

Macromolecular Materials and Engineering
www.mame-journal.de

Structuring Nanofibers of SMEC Sheets: A New Approach to Control Self-Folded Shape by Uniaxial Stretching

*Oscar Rabaux, Raphaël Riva, Ludovic Noels, and Christine Jérôme**

Shape-memory elastomer composite (SMEC) sheets, made of a honeycomb structured electrospun poly(ϵ-caprolactone) (PCL) fiber mat embedded in a silicone (PDMS) elastomer, fold on themselves upon uniaxial traction. The self-folding of the composite sheet originates from a bi-layered structure obtained by a simple one-step impregnation process. Indeed, the impregnation of a structured PCL fiber mat by oily PDMS in a flat Teflon mold leads, after curing, to an asymmetric composite sheet made of one PDMS flat thin layer on the mold side and one rough PDMS/PCL composite layer on the other side due to specific affinities between the three polymers involved. The self-folded shape of such structured single sheet obtained upon uniaxial stretching and stress release is controlled by the honeycomb pattern orientation versus stretching direction, by the pattern size and by the applied uniaxial stretching stress. High shape recovery and robust shape memory cycling are also demonstrated by dynamic mechanical analysis. This innovative process based on the mat structuration allows a straightforward one-step fabrication of shape memory sheets, with a wide scope of tunable self-folded curvatures exhibiting efficient temperature shape recovery.

1. Introduction

Inspired by the nature that takes benefits of self-folding in response to various stimuli, researchers deeply investigated the development of self-folding soft sheets especially based on polymer composites or multimaterials allowing the easy development of biomimetic systems such as the pinecone.[1,2] Self-folding of thin sheets is observed when a variation of one of the physicochemical property occurs among the sheet thickness. Various strategies for self-folding of soft sheets are considered.[3] To obtain important curvatures, polymers with large volume change due to solvent uptake have been used. Interestingly, the gradient of swelling between the layers can be obtained by multiple triggers. It starts with classical different swelling capacities because of different chemical interactions with the solvent between the layers.[4] These different interactions can be tuned by IR irradiation or changing the temperature or the pH of the solution, even leading to reversible bending because of a switch between the solvent affinity of the layers.[5–9] Another strategy is to induce a gradient of the crosslink density, either with a photomask and different time of irradiation, either with photolithography.[10–12] More straightforward, the bending can be tuned by the dimensions of the sheets and especially the ratio of thicknesses between the layers.[13] Though, important thickness variations because of solvent uptake can be a limitation for several applications. This has been overcome with mechanical actuation of the sheets. Here, a sheet made of at least two layers with different mechanical properties is requested, e.g. one plastic ply adhered to an elastic ply.[14,15] The response of each layer to elongation is thus different. After elongation and stress release, the elastic layer tries to restore its initial length while being restricted by the more plastic one. It results in a gradient of elongation along the sheet thickness, creating the bend. When shape-memory polymers (SMPs) are applied to these systems they offer in addition to store a self-folded shape, the capability to retrieve the initial flat shape upon a dedicated trigger. Indeed, SMPs are materials able to restore their initial shape (as-synthesized permanent shape) from a fixed deformed shape (temporary shape) by the action of an appropriate stimulus, such as heat or light. For example, multimaterials with polymers of different glass transition temperatures (T_g) recoil successively at tuned temperatures forming a closed box.[16] More recently two approaches to tackle the limitations of the classical SMPs such as nonelastomer properties or lack of shapes adaptability were investigated. In a first approach, porous films of a semicrystalline polymer easily stretchable due to the porosity showed shape-memory properties both at the macroscopic scale and at the scale of the porosities.[17] Beside, shape-memory elastomer composites (SMECs) were developed. These are composite materials made of an elastomer matrix (e.g., PDMS) reinforced by embedding a nanofiber mat of a semicrystalline polymer (e.g., poly-ϵ-caprolactone, PCL). In these SMECs, deformations are fixed by the embedded semicrystalline fibers preventing the elasticity of the elastomer matrix thanks to its rigidity. Shape recovery is triggered by going above the T_m of the fibers leading to the drop of the molten fiber modulus

O. Rabaux, R. Riva, C. Jérôme
Center for Education and Research on Macromolecules
University of Liège
Allée du Six Août 13, Liège 4000, Belgium
E-mail: c.jerome@uliege.be
L. Noels
Computational and Multiscale Mechanics of Materials
University of Liège
Allée de la Découverte 9, Liège 4000, Belgium

The ORCID identification number(s) for the author(s) of this article can be found under https://doi.org/10.1002/mame.202200270

DOI: 10.1002/mame.202200270

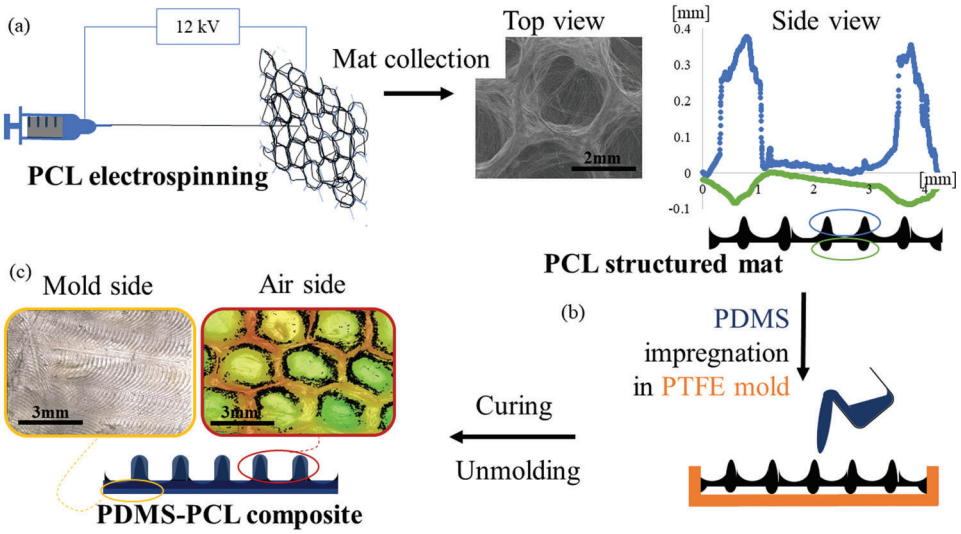

Figure 1. Scheme of SMEC sheet fabrication: a) PCL electrospinning on a honeycomb structured collector; SEM picture of the collected nanofiber mat and thickness variation of the structured PCL nanofiber mat measured by profilometry b) PDMS impregnation in a Teflon mold c) surface topography of each side of the resulting SMEC sheet measured by profilometry.

allowing thus the release of the stress on the elastomer network which comes back to its initial shape defined by the crosslinking. SMEC-based self-folding materials have been successfully prepared presenting a localized curvature. Localized heating was triggered by light absorption with a mask and induced the local curvature upon stress release.[18,19] Systems were designed by embedding fibers in an elastomeric matrix, and laminated structures with different fibers orientations in each layer made possible strong curvatures, as well as helix-like shapes.[1,20–23] The curve can be predicted by modeling the different layers in parallel.[24] This paper aims at reporting on a straightforward fabrication process for the development of a SMEC-based single-sheet able to self-fold in a wide variety of curvatures depending on the orientation of the applied uniaxial stretching. This goal is achieved by structuring the composite sheet, more precisely by giving a honeycomb pattern structure to the embedded nanofiber mat. The honeycomb geometry is selected as motif because such pattern is characterized by the highest specific strength which is highly important since it has to sustain the deformation of the composite, especially the uniaxial elongation of the elastomer matrix. In addition, this honeycomb geometry offers several symmetry axes so that different self-folded shapes can be foreseen depending on the orientation of the honeycomb versus the applied deformation. For that purpose, biocompatible semicrystalline PCL is electrospun into a honeycomb structured nanofiber mat which is then impregnated in a Teflon mold by liquid poly(dimethyl siloxane) (PDMS), precursor of the elastomer matrix.[25] Due to the affinity of the oily PDMS for the PCL electrospun mat, the developed impregnation process leads to a single sheet presenting a smooth surface of pure PDMS on one side (the mold side) and a rough surface of PDMS/PCL composite with a regular topography controlled by the honeycomb structuration of the PCL mat on the other side. Such asymmetric sheet is able to self-fold upon uniaxial stretching and stress release with various curvatures which are directly controlled by the orientation of the honeycomb hexagonal pattern versus the strain. Remarkably, upon self-folding by uniaxial stretching, this SMEC sheet forms a tube exhibiting the rough side toward the outside and the smooth surface in the lumen. Therefore, this new concept could be later applied for intravascular implants that require an external roughness to insure a good adhesion to the natural tissue and smooth surface in the lumen to prevent clotting and restenosis.[26–28]

2. Results and Discussion

2.1. Self-Folding SMEC Sheet Fabrication

The objective of the developed fabrication process is to be fast and simple, avoiding lamination and pasting of several layers. Thus, a one-step molding process is followed to obtain the targeted self-folding SMEC sheet exhibiting easily tunable self-folded curvatures upon uniaxial stretching. For this purpose, a honeycomb-structured nanofibrous mat of PCL was impregnated with PDMS in a Teflon (PTFE) mold as sketched in **Figure 1**.

2.1.1. Honeycomb Structured PCL Fiber Mat

The honeycomb motif was selected as pattern for structuring the PCL fiber mat because this continuous design is presenting the highest specific strength. Indeed, the role of the structured mat is to fix the shape of the stretched composite overcoming the elasticity of the elastomer matrix. For this purpose, PCL was electrospun as nanofibers at room temperature from a solution in a THF/DMF mixture by using a honeycomb metallic grid as collector (Figure S1, Supporting Information). Two honeycomb collectors of different size are used, referenced as small hexagons (SH), or large hexagons (LH). The edges of the hexagons being metallic, the PCL nanofibers are preferentially deposited there, even

though some fibers were also observed across the cavities (Figure 1a, SH). The difference between the number of nanofibers effectively deposited on edges or in the cavities decreases with the electrospinning time. Nevertheless, in order to reach a structured mat of significant thickness (>0.3 mm), the electrospinning was conducted for 2.5 h. To preserve preferential deposition on the edges, the voltage was increased by 1 kV every 30 min to compensate the passivation of the collector as far as nanofibers are deposited, leading to structured mats with a high density of fibers on the edges and lower density in the alveolae (Figure 1a). Scanning electron microscopy (SEM) pictures of both sides of the electrospun mat were recorded by focusing on the dense area (edges) to confirm the homogeneity of the formed fibers along the whole electrospinning process (Figure S2a,b, Supporting Information). The shape and diameter of the fibers were similar from side A (last fibers deposited) to side B (first fibers deposited), with close average diameters ($\varnothing_A = 1.38$ µm; $\varnothing_B = 1.21$ µm), and without defects. The SEM observation of the mat in the center of the alveolae (Figure S2c,d, Supporting Information) shows that the density of fibers is much smaller. No significant difference of homogeneity is evidenced between the two sides in these areas.

Interestingly, by using a larger honeycomb collector (LH) (Figure S1b, Supporting Information), the mat is thicker. There are less edges to attract the PCL, so at equivalent amount of electrospun solution, more PCL is deposited on each edge. This is shown by the profilometry profiles recorded for both sides of the mats collected either on small or large honeycomb collectors (Figure S3, Supporting Information). The blue lines represent the profiles of the collector side of the mats, while the green lines represent the profiles of the needle side and are negative only for easier reading. Indeed, these graphs give a quantitative image of the mat sideview on its whole thickness since the difference between the maxima and minima have been adjusted to the mat thickness. It shows that the mats are rough on both sides, with a more pronounced rugosity toward the collector side (Figure 1a, Figure S3, Supporting Information). This means, that despite the increase of voltage during electrospinning, the insulation effect is increased with the deposition time leading to less differences between the edges and the center of the alveolae. Finally, Figure S3 (Supporting Information) also shows that independently of the size of hexagons the mat reproduces exactly the pattern of the collector where the distances between the edges are given by Figure S1 (Supporting Information).

2.1.2. PDMS Impregnation of the Honeycomb Structured Mat

To obtain the SMEC sheet, the honeycomb-structured PCL fiber mat has to be embedded in the PDMS elastomer matrix (Figure 1b). As shape memory properties are foreseen, the PCL content of the final composite sheet has to be high enough to be able to fix the temporary shape of the sheet. Nevertheless, reaching the complete coverage of the PCL fibers by PDMS is mandatory to keep the fiber morphology when the PCL is molten during the shape memory cycle. This imposes a minimum limit below which the amount of PDMS to be used cannot be lowered. To fulfill both antagonistic requirements, we determined by trials and errors that the optimal PCL content in the final composite sheet is 8 wt%. The full coverage of the PCL by PDMS was confirmed by the disappearance of the ester band typical for PCL in the IR-ATR spectrum recorded on the composite (Figure S4, Supporting Information). The low content in PCL is due to the large unoccupied volume by the nanofibers in the electrospun mat with especially low density in the centers of the alveolae and also because of different affinities with the mold as it will be seen further on. In comparison, the optimal composition with random fibers found by Mather et al was around 25%.[29]

A dedicated impregnation process was developed (for the details see Section 4) in order to provide a SMEC sheet where all PCL fibers are coated by the PDMS. For that purpose, half of the total amount of liquid PDMS is first poured in a Teflon mold having a smooth surface. Then, the PCL structured mat that was cut to fit the mold dimensions is placed lying in the mold. Finally, the second half of PDMS is poured on top (Figure 1b). Vacuum is applied at each PDMS addition and before curing in order to remove any air bubbles possibly entrapped to avoid structural defects in the elastomer which would lead to failure under stress application. Since PDMS wets very well PCL (contact angle = 21 ± 3° in air atmosphere), it spreads easily over the nanofibers insuring their complete coating. The curing temperature was set at 40 °C to ensure that PCL does not melt during the procedure not to lose the structure of fibrous PCL and sheath of crosslinked PDMS. This process preserves on the air side the topography of the embedded mat as it can be seen on Figure 1c. In contrast, PDMS is spreading even better over Teflon (contact angle <5°), and therefore a smooth thin layer of PDMS is templated by the Teflon mold surface on the other side of the sheet (Figure 1c). SEM image of the cryo-fractured composite sheet (**Figure 2**a) also shows the smooth surface (placed on top) and the thickness variation on the other side (highlighted by added dotted line on the picture). Picture at higher magnification (Figure 2c) shows that PDMS (grey matrix) is fully embedding the PCL nanofibers that are buried or that were extracted from the matrix during the fracture letting visible bright circular holes on the grey PDMS matrix.

Following this easy process, the resulting sheet is thus a thin elastomer composite single sheet (≈500 µm for SH and ≈800 µm for LH), exhibiting different topographies on both sides as observed on SEM images with a thin flat PDMS layer on the mold side.

The different topographies were confirmed by recording 3D mode profilometry images consisting in a color gradient function of the height of the topography of both sides of the sheet. Such image recorded on the air side shows a marked roughness reproducing the regularity of the honeycomb structure of the embedded mat (Figure 1c, air side). On the image recorded on the mold side (Figure 1c, mold side), the absence of color contrast reveals a smooth surface with small asperities coming from defaults of the mold. These are nevertheless too small to be detected in the 2D profiles.

Analysis of the 2D profile of the air side allows to more precisely quantify the height differences between the edges and the center of alveolae of the regular honeycomb roughness (**Figure 3**—dark blue lines).

Finally, 2D profiles also reveal that the roughness of the composite sheet is independent on the way the asymmetric PCL mat is deposited in the mold (rougher side of the mat up or down). Indeed, Figure 3b shows that applying the impregnation process by flipping the asymmetric PCL mat upside down leads to the same

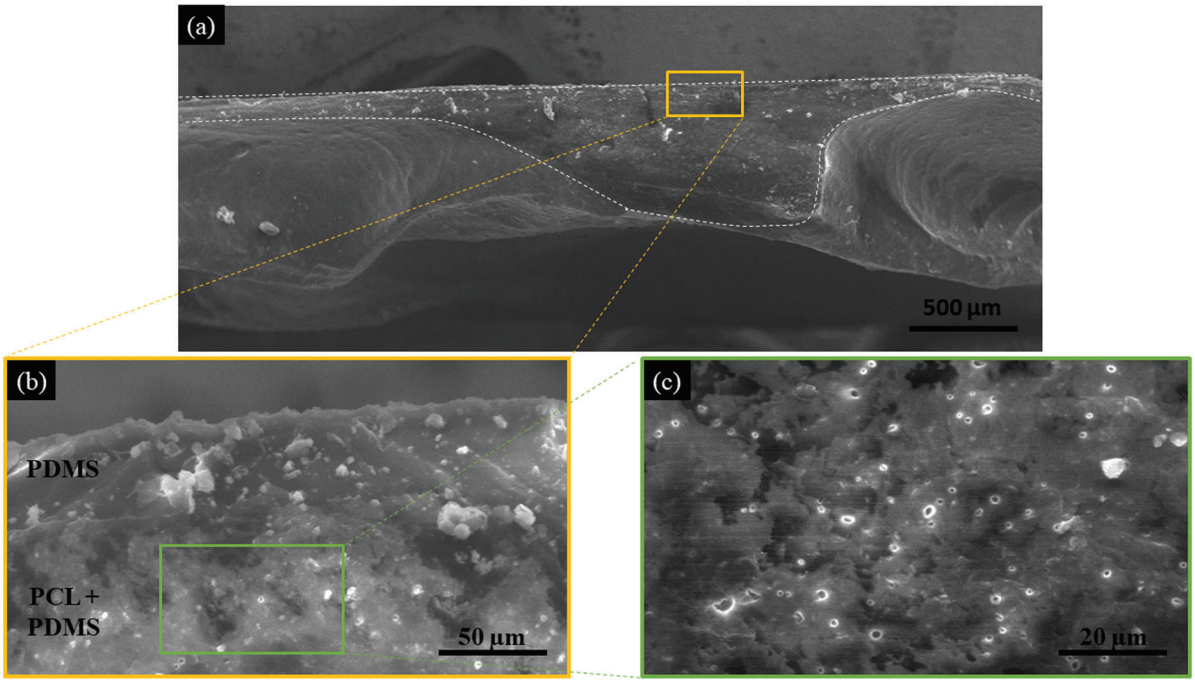

Figure 2. SEM side views of a cryo-fractured structured SMEC sheet showing the morphology of a) the full thickness of the SMEC sheet, b) the surface layer on the mold side, and c) the PDMS embedding PCL fibers.

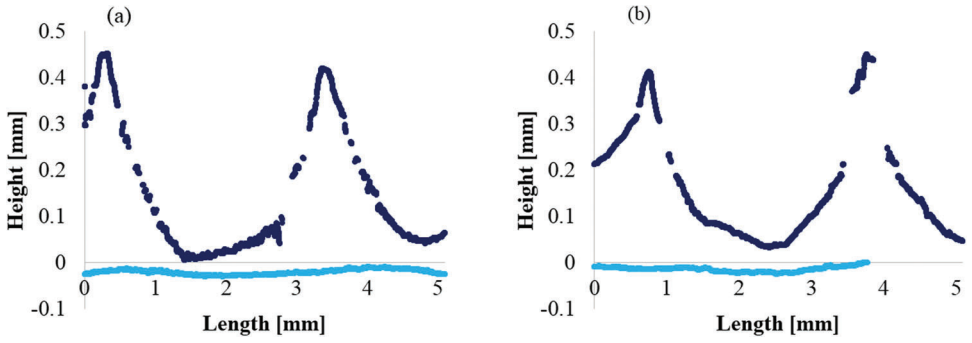

Figure 3. 2D profiles of both sides after impregnation and curing for SMEC sheets prepared by placing the honeycomb-mat in the mold with a) face A up or b) face B up.

profiles as in Figure 3a, with sheets of the same thickness. The structuration and composition of the sheet along the thickness in both impregnation systems were further analyzed by SEM of the cryo-fractured sides as shown in Figure S5 (Supporting Information). Similar thicknesses of the PDMS ply (≈75 µm and ≈65 µm respectively) representing 70% and 60% of the height in the center of the hexagons and 14% and 13% of the height at the edges were observed. This observation is most probably due to the soaking around the fibers in the centers of the hexagons, which are then attracted toward the bottom of the mold because of gravity. It proves that it is possible to consider the process side-independent on the mat deposition despite its asymmetry.

The combination of structured electrospun mats, wettability of the pre-cured resin and the mold material made possible to get composite materials with two different types of topographies for each side, and which chemical composition is already known to have shape-memory properties.[29] In summary, this process has many advantages compared to reported layer by layer fabrication allowing time-efficiency, low cost, absence of delamination, and small thickness.

2.2. Temporary Shape Self-Folding by Uniaxial Stretching

2.2.1. Self-Folding Observation and Origin

When a sample (30 mm × 10 mm × 0.5 mm) of the SMEC sheet is elongated up to 80%, self-folding is observed upon stress-release (**Figure 4**a). This is due to the strain recovery mismatch between the fully elastic thin PDMS layer present on the smooth side of the sheet (Figure 2b) and the plastic PCL/PDMS composite layer on the rough side. Two control samples were designed to en-

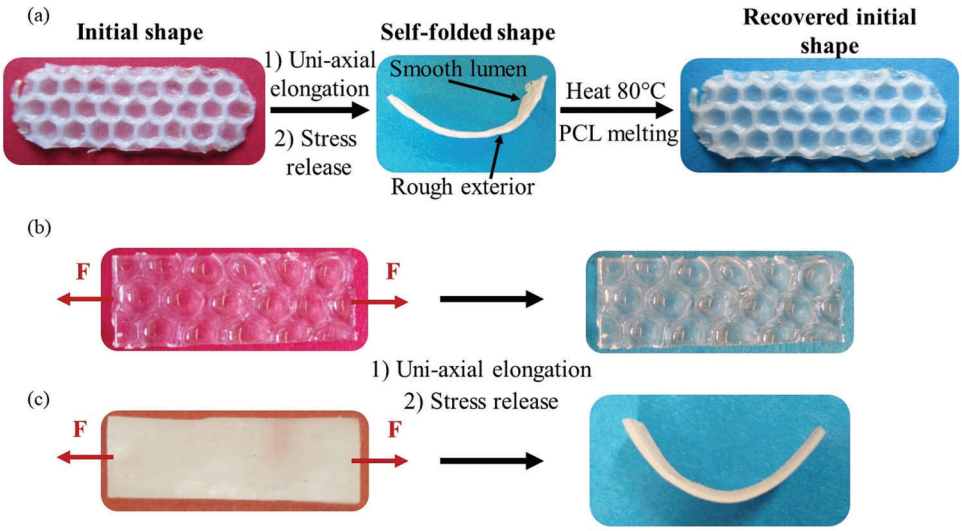

Figure 4. a) Self-folding and shape memory of the structured SMEC sheet and behavior of control samples. b) Structured silicone (C1) and c) nonstructured SMEC (C2) after uniaxial traction and stress release.

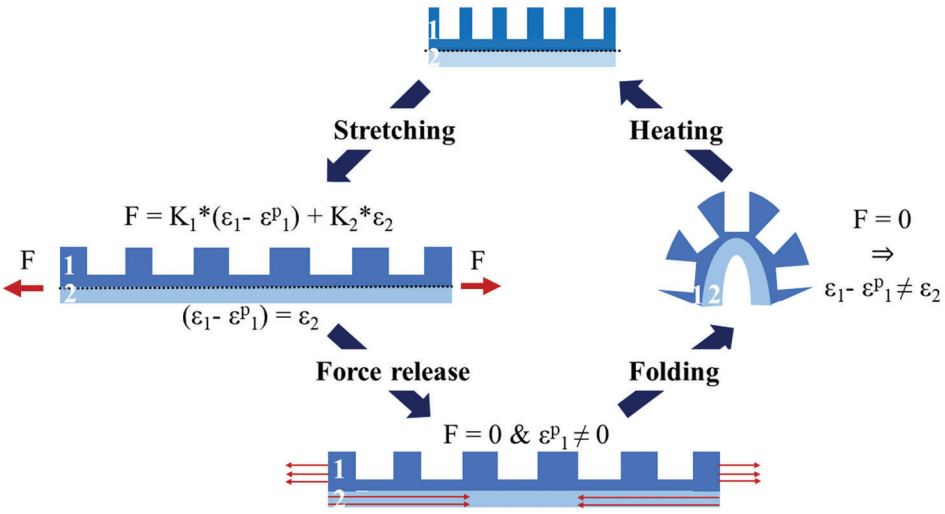

Figure 5. Scheme of the mechanism of folding and shape-memory recovery with ϵ_i the strain of the ith layer, $\epsilon^p{}_1$ the residual strain and $K_i = E_i \times S_i$, E_i being the Young modulus of the ith layer and S_i its specific surface.

sure that this self-folding phenomenon comes from the chemical composition of the composite and that it was independent on the topography of the shape-memory layer. A sample made of silicone only (C1, Figure 4b) shows that even though it presents an asymmetry in roughness on both sides, it is fully elastic and thus not able to store a deformation. So, it comes back to its initial length and shape upon unloading, despite the different surface topographies. The control sample C2 (Figure 4c) was fabricated from a randomly deposited nanofibers mat, which was intrinsically flat on both sides because the charged solution was homogeneously attracted by the collector leading to no heterogeneities in the thickness. Thus, the final composite was also flat on both sides. The process of fabrication being the same as for the SH, here again the affinity between PDMS and Teflon is responsible for a thin layer of PDMS underneath the composite ply, representing around 18% of the total thickness (Figure S6, Supporting Information). After uniaxial elongation and stress-release, this sample also folds on itself showing that the rugosity of the SH is not fully responsible of the folding phenomenon, even though it might partially impact it due to thickness heterogeneity. The presence of a full PDMS thin layer at the mold side exempt of PCL nanofibers and thus fully elastic is rather responsible of the sheet folding.

This self-folding process is sketched on **Figure 5** where the light blue part (layer 2) would represent a homogeneous and fully elastic PDMS thin layer while the dark blue part (layer 1) would

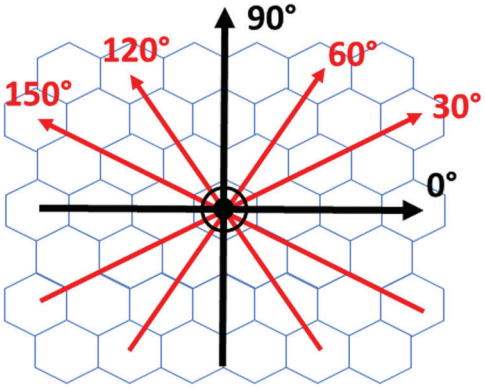

Figure 6. Symmetry axes of the honeycomb structure.

stand for the PDMS/PCL composite. Upon uniaxial stretching, both layers are stretched equivalently ($\varepsilon_1 - \varepsilon_1^p = \varepsilon_2$). However, after stress release the PCL nanofibers induce a permanent deformation of layer 1, also called residual strain ($\varepsilon_1^p \neq 0$). As the PDMS network is continuous over the whole sample due to the fabrication process, the elastic layer exerts a compressive force on the PCL-PDMS layer, while this layer exerts a tensile force resulting in a bending moment folding the sheet (Figure 5). Accordingly, the smooth side of the sample is always exposed toward the interior of the self-folded shape. Finally, the thinner the material the more folded at equivalent elongation, because the flexural rigidity depends on the thickness at the power three according to the classical theory for thin plates, while the forces vary with the thickness.[30] This is the reason for our objective to obtain self-folding without lamination which increases the thickness, representing 16% of the total thickness in the bilayer systems of Robertson et al.[23] Figure 4a shows the recovery of the initial shape upon heating. Indeed, above the melting temperature, the PCL fibers become a viscous liquid in the PDMS channels and do not exert anymore the force storing the deformation. The elasticity of the PDMS network allows then the complete recovery of the initial shape.

2.2.2. Effect of Honeycomb Orientation on Self-Folding Behavior

In this study, our objective was to obtain a material exhibiting a variety of self-folded shapes in function of the direction of the applied uniaxial tensile stress. For that purpose, the PCL nanofiber mat was structured with a honeycomb pattern offering several symmetry axes (**Figure 6**).

We have first investigated the effect of the honeycomb orientation toward the uniaxial stretching direction on the self-folding. In order to keep all parameters the same (composition, thickness) excepted the honeycomb orientation, all the samples were cut from the same large SMEC sample of 10 cm × 10 cm but along different axes. **Figure 7** (samples SH-0° to SH-30°) shows the various tested sample orientations (from 0° to 30°) and the corresponding self-folded temporary shapes obtained after elongation at 120% and stress release.

Clearly, the initial orientation of the honeycomb has a strong influence on the obtained self-folded shape. Indeed, a different direction of the honeycomb pattern leads to various curvatures at equivalent strains. Thanks to the elastomeric behavior of the PDMS matrix and to the PCL reinforcement which prevails early failure, the curvatures can be very stiff as it can be seen in Figure 7 because the sheet can be highly stretched (up to 150% at room temperature).

This honeycomb orientation versus elongation direction dependence of the self-folding was further analyzed quantifying the curvature (**Figure 8**). For that purpose, we determined the one-dimensional $\bar{\kappa}$ parameter (see the Experimental Section for details) to obtain quantitative data of the curvature of the self-folded samples toward the averaged monodirection of folding which is not necessarily the exact direction of traction. The data corresponding to the samples shown on Figure 7 are displayed in Figure 8 for a strain of 120% (dotted circle).

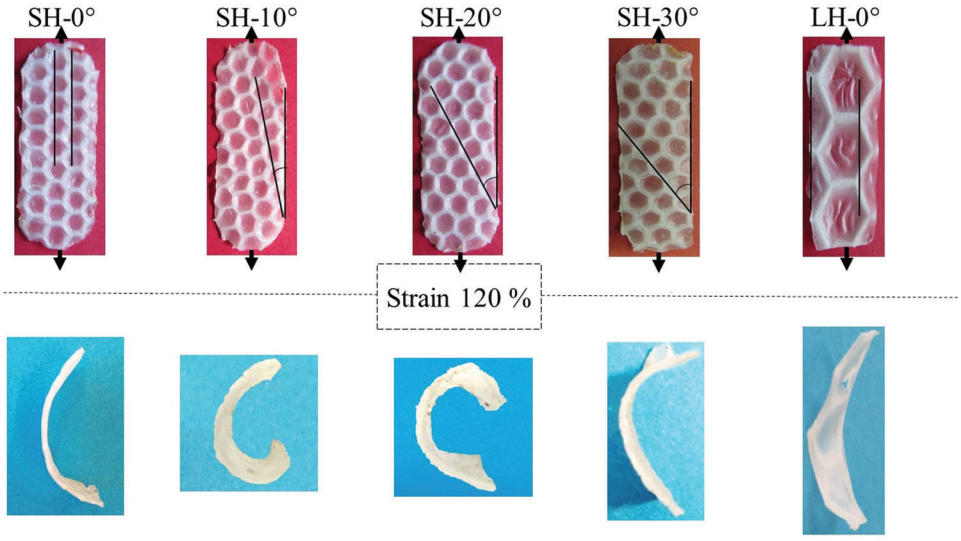

Figure 7. Effect of honeycomb orientation toward uniaxial stretching direction on the self-folded shape. Pictures up: before uniaxial tension; pictures down: after 120% elongation and stress release.

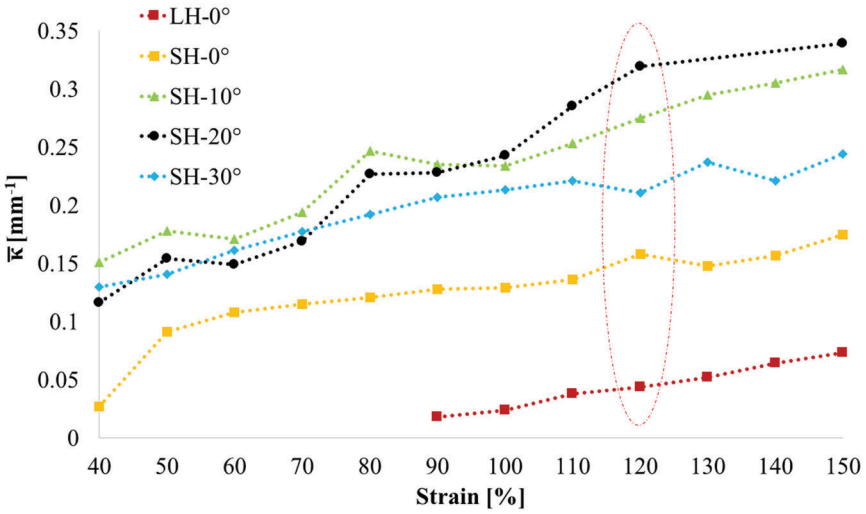

Figure 8. Curvature ($\bar{\kappa}$) of the self-folded SMECs in function of the orientation of the strain (SH-0° to SH-30°), of the strain intensity (%), and of the honeycomb size (SH-0° vs LH-0°).

Figure 8 shows that at high strains (>100%) the curves of SH-10° (green curve) and SH-20° (black curve) are close, while SH-0° and SH-30° have lower values of $\bar{\kappa}$. This behavior with on one side low curvature at SH-0°, SH-30° and on the other side highly curved sample at SH-10°, SH-20° can be explained by symmetry considerations of the honeycomb structure as shown in Figure 6.

Indeed, the ply of our composite material with the honeycomb reinforcement can be modeled as a repetitive hexagonal cell with perfectly aligned fibers along the edges of the honeycomb pattern. This consideration allows to describe the ply as a particular case of an orthotropic material. Indeed, the honeycomb pattern has three symmetry axes which are orthogonal, two of them being represented in black in Figure 6. It is referred as a particular case of orthotropy due to the regular hexagonal structure which also has four supplementary axes of symmetry represented in red in Figure 6. Though, it is a repetitive pattern and the intern angles of the hexagons are all 120° (Figure S2, Supporting Information) such that axes at 0°, 60°, and 120° as well as axes at 30°, 90°, and 150° cannot be distinguished, respectively. Finally, there are two extrema with the so-called zigzag (corresponding to 0°) and armchair (corresponding to 30°) directions, and intermediate ones in between 0° and 30° which are the two first occurrences of the extrema.

In any orthotropic ply, the general in-plane elastic mechanical behavior is given by Equation (1) linking the resultants $n_{\alpha\beta}$ and the moments $m_{\alpha\beta}$ to the strains $\varepsilon^0_{\alpha\beta}$, $\gamma^0_{\alpha\beta}$ and the curves $\kappa^0_{\alpha\beta}$ with the coefficients $A_{\alpha\beta\gamma\delta}$, $B_{\alpha\beta\gamma\delta}$, and $D_{\alpha\beta\gamma\delta}$ given by Equations (2)–Equation (4), respectively[31]

$$\begin{pmatrix} n_{xx} \\ n_{yy} \\ n_{xy} \\ m_{xx} \\ m_{yy} \\ m_{xy} \end{pmatrix} = \begin{pmatrix} A_{xxxx} & A_{xxyy} & A_{xxxy} & B_{xxxx} & B_{xxyy} & B_{xxxy} \\ A_{yyxx} & A_{yyyy} & A_{yyxy} & B_{yyxx} & B_{yyyy} & B_{yyxy} \\ A_{xyxx} & A_{xyyy} & A_{xyxy} & B_{xyxx} & B_{xyyy} & B_{xyxy} \\ B_{xxxx} & B_{xxyy} & B_{xxxy} & D_{xxxx} & D_{xxyy} & D_{xxxy} \\ B_{yyxx} & B_{yyyy} & B_{yyxy} & D_{yyxx} & D_{yyyy} & D_{yyxy} \\ B_{xyxx} & B_{xyyy} & B_{xyxy} & D_{xyxx} & D_{xyyy} & D_{xyxy} \end{pmatrix} * \begin{pmatrix} \varepsilon^0_{xx} \\ \varepsilon^0_{yy} \\ \gamma^0_{xy} \\ \kappa^0_{xx} \\ \kappa^0_{yy} \\ \kappa^0_{xy} \end{pmatrix} \quad (1)$$

which can be rewritten as $\begin{pmatrix} n \\ m \end{pmatrix} = \begin{pmatrix} A & B \\ B & D \end{pmatrix} * \begin{pmatrix} \varepsilon^0 \\ \kappa^0 \end{pmatrix}$

$$A_{\alpha\beta\gamma\delta} = \sum_i C^i_{\alpha\beta\gamma\delta} * t_i \text{ with } C^i_{\alpha\beta\gamma\delta}$$

the adapted elastic moduli and t_i the thickness of the ith ply (2)

$$B_{\alpha\beta\gamma\delta} = \sum_i C^i_{\alpha\beta\gamma\delta} * t_i * \bar{z}_i \text{ with } \bar{z}_i$$

the relative height of the ply compared to the medium plane (3)

$$D_{\alpha\beta\gamma\delta} = \sum_i C^i_{\alpha\beta\gamma\delta} * \left(t_i * \bar{z}_i^2 + \frac{t_i^3}{12} \right) \quad (4)$$

In our case, the coefficients $C^i_{\alpha\beta\gamma\delta}$ can be derived from Gibson and Ashby equations for a honeycomb structure.[32] Though, these are approached equations with the hypothesis of empty hexagons with edges of bulk material, thus we preferred to demonstrate the observed phenomenon with general theoretical considerations.

The composite sheet can be approximated by the stacking of an isotropic layer and an orthotropic layer such that the mechanical properties are dependent on the direction of loading. The orthotropic ply is made of PCL and PDMS such that it is necessary to add a plastic component in Equation (1) to model the residual strain of this ply upon stress release, leading to Equation (5)

$$\begin{pmatrix} n \\ m \end{pmatrix} = \begin{pmatrix} A & B \\ B & D \end{pmatrix} * \begin{pmatrix} \varepsilon^0 \\ \kappa^0 \end{pmatrix} - \begin{pmatrix} n^p \\ m^p \end{pmatrix} \quad (5)$$

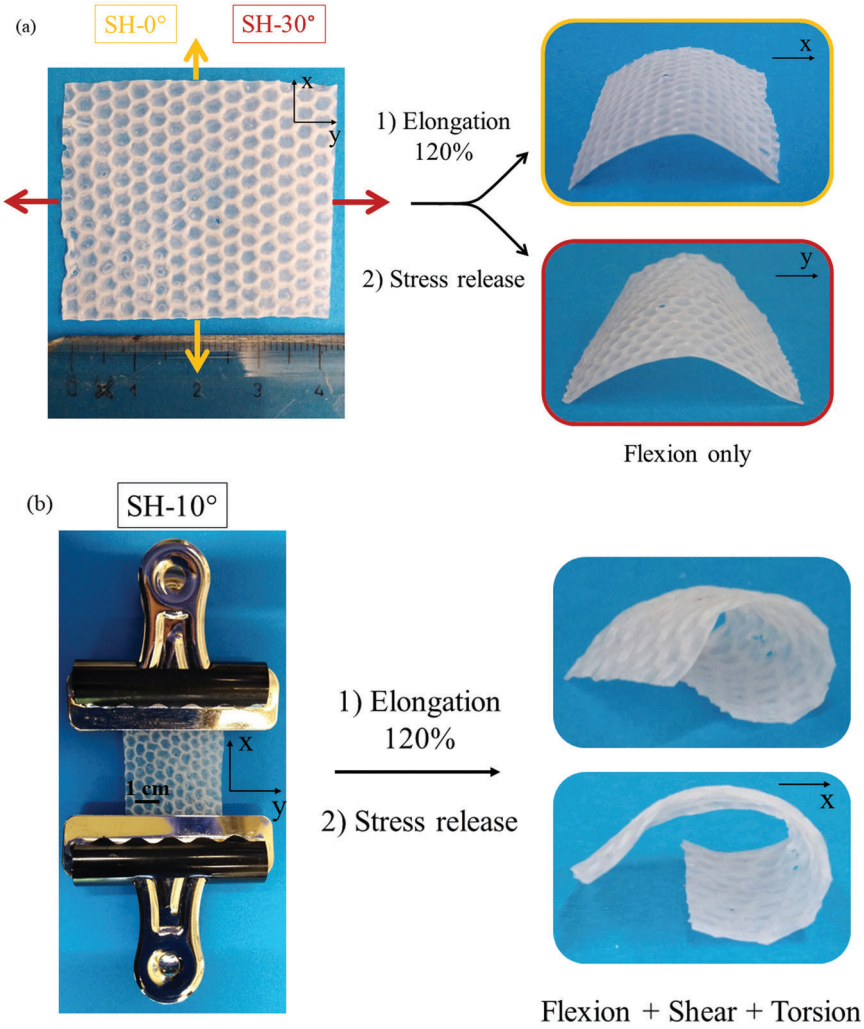

Figure 9. Different components in the curvature if the stretching axis is either a) a symmetry axis of the honeycomb pattern or b) an axis in between the two distinct axes of symmetry of the honeycomb pattern.

Upon stress release, at equilibrium, $\begin{pmatrix} n \\ m \end{pmatrix} = \begin{pmatrix} 0 \\ 0 \end{pmatrix}$ guiding to Equations (6) and (7)

$$A*\varepsilon^0 + B*\kappa^0 = n^p \tag{6}$$

$$B*\varepsilon^0 + D*\kappa^0 = m^p \tag{7}$$

First, as the composite sheet is not a symmetric stacking of two plies, it is known that a uniaxial tensile stress will induce flexion with the terms $C^i_{\alpha\beta\gamma\delta}$ in $B_{\alpha\beta\gamma\delta}$ which do not compensate with the relative heights, such that $B \neq 0$. This means that the curvature comes from the coupling of the plastic resultant and moment of the composite ply.

Then, a uniaxial loading at 0° and 30° (≡90°) as considered in Figure 8, does not induce a coupling traction/shearing because these are the axes of symmetry of the orthotropic ply. In this case, the components A_{xxxy}, A_{yyxy}, A_{xyxx}, and A_{xyyy} are null. When the loading direction is in between these symmetry axes, e.g., at 10° or 20°, these terms are not null and are responsible for a coupling between traction and shear.

Moreover, it is known that the terms corresponding to the coupling bending/torsion are D_{xxxy}, D_{yyxy}, D_{xyxx}, and D_{xyyy} such that the coefficients $C^i_{\alpha\beta\gamma\delta}$ are the same than those involved for the coupling traction/shear. Finally, it is understandable that for loads at 10° or 20°, the bending and the shearing induce torsion while at 0° and 30° the absence of shearing is also responsible for the absence of torsion. This phenomenon is well observed with sufficiently large samples (4 cm × 4 cm) in **Figure 9**.

This explains the greater curves at 10° and 20° compared to 0° and 30°, because with such samples we were able to measure only the average curvature in one direction. This addition of shear and torsion at 10° and 20° makes the measured 1D averaged curvature $\bar{\kappa}$ higher.

Figure 9a shows that due to the traction along the symmetry axes only a flexion mode is on, and the curvature follows one direction being the direction of stress. Figure 9b shows that due

to the traction along an intermediate axis, flexion, shear, and torsion modes are on, and it is possible to define several curvatures in different directions. Interestingly, when the lateral dimension of the samples is small, the flexion mode shows a major contribution to the resultant curvature as shear and torsion could not be well detected visually.

The difference between SH-0° and SH-30° (Figure 8) comes from the difference of alignment of the hexagons (Figure 7). Globally, at 0°, more edges are perpendicular to the traction axis compared to 30°. Rodriguez et al showed that the shape fixity of a SMEC sheet was dependent on the direction of the fibers compared to the traction axis, decreasing when it is more and more perpendicular.[33] Thus, at 0° the elastic return force in the shape-memory layer is more important because less edges of fibers can retain the deformation. The gradient of strain recoveries is smaller, which explains the smaller curvature of SH-0°.

For the possible application as intravascular implants, achieving a tubular self-folded shape (meaning $L_r = 0$ and $\alpha = 360°$) penetrating easily in the blood vessels and able to cover the vessels inner wall upon shape recovery would be targeted. This goal could be achieved by adjusting the size of SH-10° and SH-20°, since samples of 15 mm and 150% strain come already very close to this value ($\alpha \approx 300°$ and 320° respectively) (Figure S7, Supporting Information).

2.2.3. Effect of the Honeycomb Size on Self-Folding Behavior

As evidenced in the impregnation section, in LH sheet, the proportion of the composite layer is more important as compared to the thin PDMS layer obtained on the mold side, thus the spring-back effect of PDMS is decreased for LH as compared to SH sheets. This is confirmed by the lower curvature, i.e., lower $\bar{\kappa}$ value of 0.04 mm^{-1} for LH-0° compared to 0.16 mm^{-1} for SH-0° (Figures 7 and 8).

2.2.4. Effect of the Strain on Self-Folding Behavior

Figure 8 also shows that $\bar{\kappa}$ increases when the strain increases whatever the honeycomb orientation. This is due to the shape-memory layer which residual strain increases with the strain due to the plastic behavior of the PCL fibers. Thus, the difference of strain recovery between the layers and the curvature is more and more important.

In summary, the objective of having a material with a direction dependent self-folding thanks to the structuration of the PCL mat was fulfilled. It was also ensured that this does not originates from deformation inhomogeneities upon stretching as it was discussed by studies from Li and Shimomura,[34–35] and as evidences by Figure S8 (Supporting Information) showing the deformed motifs upon stretching in the two symmetry axes of the honeycomb pattern.

2.3. Shape Memory and Reproducibility

The samples fulfilled both requirements for shape-memory properties namely a chemical network (crosslinks of PDMS) to fix the permanent molded shape and a physical network (crystallites of PCL) to fix the deformations. The melting of the PCL crystallites is thus the trigger for shape recovery. To ensure a reproducible crystallization between each cycle, the sample was cooled at 3 °C min^{-1} down to 0 °C representing a gap with T_m close to what was recommended by Li and coworkers for an optimal growth of the crystallites to fix the deformed shapes.[36]

The shape-memory properties of the different samples were tested with a dynamic mechanical analyzer (DMA), with 3 cycles following a classical procedure detailed in Section 4. Because of self-folded temporary shapes, the shape-memory ability was mainly quantified with the recovery ratio calculated as defined in Equation (8)

$$R_{\text{recovery}}\ (N) = \frac{\varepsilon_{\max} - \varepsilon_h\,(N)}{\varepsilon_{\max} - \varepsilon_h\,(N-1)} \tag{8}$$

where ϵ_{max} is the maximum strain after the stress ramp and $\epsilon_h(N)$ is the strain after reheating the sample at the cycle N.

In **Figure 10**, displaying the shape-memory cycles of SH-20°, the black line represents the first cycle, the red the second cycle and the yellow the third cycle. First, what is striking with this graphic is how reproducible the cycles are, excluding the classical training phenomenon in the first stress ramp.[37] This testifies again of the complete impregnation of PCL fibers by liquid PDMS, and the efficient curing of PDMS into a network able to prevent the flowing of PCL once melted even under stress.

The stress ramp was slightly adjusted to achieve around 80% of strain as maximum strain. Due to the self-folding, the strain after stress release goes down to −23% for the 3 cycles traducing the reproducibility of the self-folded shape. The calculated shape recovery is superior than 0.99 and does not decrease after 3 cycles.

All the other tested samples showed the same ability for shape recovery and reproducibility (Figure S9, Supporting Information). Between the cycles of the SHs the only difference is the strain just after the unloading of the stress, according to the angle dependent folding of the sheet described above. DMA also allows quantifying the sample curvature by mechanically unfolding the sample to measure its linear length at 0 °C. This has been done by applying a final stress ramp at 0 °C, before the last reheating, and it is represented by the thick blue line in Figure 10 and Figure S9 (Supporting Information). For this final stress ramp, two different regimes are observed: a first one characterized by a small force needed to increase the strain corresponding to the material unfolding. The second regime for which the slope is deeply decreased corresponds to a classical stress-strain regime depending on the mechanical properties of the sample at 0 °C. The breakage between these two regimes allowed us to quantify the linear elongation of the material and finally its curvature. The results of the $\bar{\kappa}$ values for the SHs during the DMA cycles are reported in Table 1 and are compared to the curvatures obtained at 80% elongation without prior melting of the PCL fibers. It shows that the folding is also process dependent. This is first due to the clamps maintaining the samples in the DMA which mitigate shearing and torsion, in comparison to the tensile tester where the samples were unmounted for measurements. Also, because of prior melting in the DMA, the final elongated shape does not depend on the PCL which adapts afterward during the crystallization. This is respon-

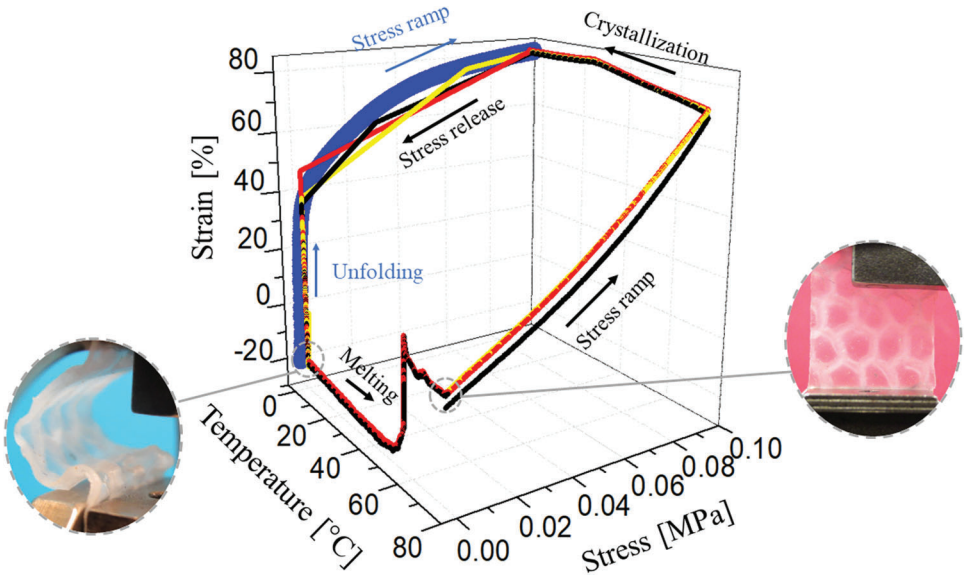

Figure 10. DMA cycles of SH-20° and final traction at low temperature to unfold mechanically.

Table 1. Curvatures obtained after 80% strain with or without prior melting.

Sample	$\bar{\kappa}$ [mm^{-1}] (Melting—80%—DMA)	$\bar{\kappa}$ [mm^{-1}] (No Melting—80%—Tensile tester)
SH-0°	0.13	0.12
SH-10°	0.18	0.25
SH-20°	0.22	0.23
SH-30°	0.16	0.18

sible for reducing the differences between all geometries for the as measured curvatures.

3. Conclusion

Composite sheets exhibiting tunable self-folding were obtained thanks to a new approach relying on the structuration of a thermoplastic nanofiber mat embedded in an elastomer matrix. By using a honeycomb metal grid as collector for electrospinning, mats of PCL reproducing the honeycomb structure are obtained. Taking advantage of the favorable wettability of PDMS for both PCL and Teflon, impregnation of these mats with PDMS in a Teflon mold and curing leads to asymmetric composite sheets exhibiting a thin smooth PDMS layer on the mold side and a composite layer with a regular roughness on the other side. This thickness heterogeneity induces strain recovery mismatch between both sides of the sheet, leading to self-folding upon stress release. Depending on the orientation of the uniaxial tension toward the edges of the hexagons, the curvature of the self-folded sheet is more or less important because of different combination of bending, shearing, and torsion modes. Self-folding also depends on the size of the hexagonal structure and increases with the strain.

These sheets containing 8 wt% of PCL exhibit excellent shape-memory recovery, and cycle to cycle reproducibility due to the complete coverage of the PCL mat by PDMS and to the peculiar honeycomb structure reinforcing the elastomer.

In summary, the structuration of the nanofibers allows to obtain self-folding materials in a one-step procedure, thin enough as they are not post-laminated, and with strong tailorable curvatures with asymmetric roughness. Those characteristics led us to believe that this new concept could advantageously be applied in the field of smart intravascular implants.

Indeed, the rough side of the self-folded sheet facing always the outside and the smooth side thus the inside, these smart sheets would perfectly fit the antagonistic requirements for intravascular implants, i.e., to present i) a strong adhesion to the vessels epithelium promoted by the rough surface and ii) a flat surface toward the vessels lumen to avoid fluids flow perturbation and cells adhesion and so prevent late thrombosis and restenosis.[28,38–42] Optimization of the self-folding and roughness of the sheets can be envisioned by notably reducing the size of the honeycomb structure. A model predicting the self-folded geometry in function of strain and initial size of the composite sheet could be developed as a tool for surgeons in line with the personalized medicine philosophy.

4. Experimental Section

Composite Fabrication: PCL (Aldrich) with an average molar mass of 80 kg mol^{-1} was dissolved in a weight equivalent mix of tetrahydrofuran (THF) (VWR) and dimethylformamide (DMF) (Acros Organics) to obtain a 15 wt% PCL solution. This solution was electrospun (ND-ES electrospinning) on a honeycomb structured metallic collector for 2.5 h with a flow rate of 13 µL min^{-1}, upon a voltage of 12 kV, at a distance of 17 cm and at room temperature. The voltage was increased at the rate of 1 kV every 30 min. The collected electrospun mat was put at 40 °C for 24 h for further evaporation of remaining solvents. The central part of the mat was cut along the shape of the mold (10 cm × 10 cm). Poly(dimethyl siloxane) (Sylgard 182—Dow Corning) mixed with its curing agent (10:1) was deposited into a poly(tetrafluoroethylene) (PTFE) mold so it represented half of the

PDMS necessary to get an 8 wt% PCL to PDMS composite. This PDMS was put under vacuum for 10 min. The PCL mat was deposited on the PDMS and after 15 min the second half of PDMS was added on the mat, put under vacuum for 30 min, and cured for 4 d at 35 °C at atmospheric pressure.

Reference Sample Fabrication: For C1, oily PDMS was poured onto the Teflon mold and the honeycomb metallic collector was pressed at the surface of the deposited PDMS during curing, which occurred at 150 °C for 15 min. Due to the very low wettability of PDMS toward the aluminum of the collector, the imprinted honeycomb roughness was in the same way as for the composites. The other side was flat again due to the affinity between PDMS and Teflon.

For C2, the same procedure described in the section "Composite Fabrication" was followed, only changing the honeycomb collector by a flat sheet of aluminum for the PCL deposition.

Scanning Electron Microscopy: Samples were gold sputtered under vacuum and a flux of argon with an electric current of 30 mA. The images were recorded with an FEI ESEM Philips XL30 in the Secondary Electron mode. The images were then analyzed with ImageJ software. A total of 100 measures on three different images were used to measure the average fiber diameter.

Differential Scanning Calorimetry: Thermograms were recorded using a TA DSC 250 calibrated with indium. For the composites, two cycles were recorded at a heating/cooling rate of ± 5 °C min^{-1} in between 0 and 100 °C. The determination of the crystalline ratio was done using Equation (9) adapting to the known PDMS-PCL ratio:

$$\%\text{crystallinity} = \frac{\Delta H_f^{obs}}{\Delta H_f^c} \times 100 \quad (9)$$

with ΔH_f^{obs} the enthalpy of fusion of the tested material and ΔH_f^c the theoretical enthalpy of fusion of PCL if it was 100% crystalline (ΔH_f^c = 139.5 J g^{-1}).[43]

Fourier Transformed InfraRed: A Thermo Scientific iD5 ATR was used to analyze the chemical composition at the surface of the composites.

Profilometer: Alicona Infinite Focus was used with the coaxial light and a magnification of x5 to characterize the topographies of both sides of each sample. 3D boxes were created and the camera found for each (*x*,*y*) coordinates the height at which the resolution was the clearest, giving the relative height of the surface. The vertical resolution was <410 nm. The lateral resolution was around 7.83 µm. The software used for 3D images and 2D profiles are Alicona MeasureSuite 5.3.1. and Alicona Laboratory Measurement Module 6.6. Because of transparent PDMS, both surfaces had to be metalized with the same procedure than with the SEM analysis.

Dynamic Mechanical Analysis: Shape-memory properties and curvatures were measured with a DMA Q800 (TA Instruments) using the tensile film clamp in controlled force mode. The sample dimensions were 20 mm × 10 mm × 0.5 mm. The sample was first equilibrated at 75 °C for 5 min and then a tensile stress ramp (up to 80% elongation) was applied. Subsequently, the sample was cooled down, under stress at 3 °C min^{-1} to 0 °C and maintained at that temperature for 5 min. The stress was finally released and the sample was reheated, stress-free at 3 °C min^{-1} to 75 °C. This process was cycled three times. Prior to the last reheating, the sample was stretched up to 0.1 MPa at 0 °C to unfold the material and retrieve the linear length needed for the calculation of the curvature.

Uniaxial Stretching: Curvatures were also measured by hand using an Instron 5566 on tensile mode. The samples (20 mm × 10 mm × 0.5 mm) were stretched up to a given elongation at room temperature. For tensile tests, the samples were elongated at 0.03 MPa min^{-1}.

Curvature Calculation: To calculate the curvature, the approximation of a unique curvature was made, which is met as long as the curved sample does not overcome one turn on itself ($\alpha < 2\pi$) (Figure S10, Supporting Information).

Two different lengths were measurable easily (**Figure 11**): the linear length of the curved material L_a and the length between the extremities named L_r and measured with the ImageJ software.

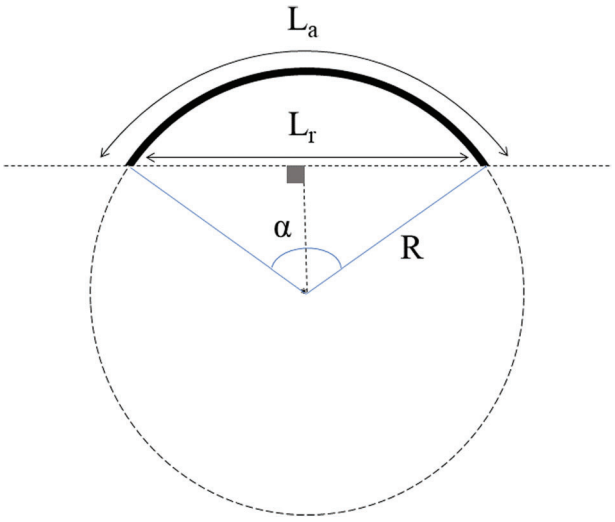

Figure 11. Scheme of the measurement of the curvature $\bar{\kappa}$.

According to Equations (10) and (11), L_a, L_r, and the average curvature $\bar{\kappa}$ which is the inverse of the radius of the theoretical circle fitting the curved sample in Equation (12) were linked

$$L_a = \alpha * R \quad (10)$$

$$\frac{L_r}{2R} = \text{SIN}\left(\frac{\alpha}{2}\right) \quad (11)$$

$$\frac{L_r * \bar{\kappa}}{2} = \text{SIN}\left(\frac{L_a * \bar{\kappa}}{2}\right) \text{ with } \bar{\kappa} = \frac{1}{R} \quad (12)$$

Supporting Information

Supporting Information is available from the Wiley Online Library or from the author.

Acknowledgements

The authors would like to thank the Department of Engineering of the University of Liège to give access to the profilometer. The authors thank the "Actions de recherche concertées 2017 – Synthesis, Characterization, and MultiScale Model of Smart composite Materials (S3CM3) 17/21-07" financed by the "Direction générale de l'Enseignement non obligatoire de la Recherche scientifique, Direction de la Recherche scientifique, Communauté française de Belgique, et octroyées par l'Académie Universitaire Wallonie-Europe" for supporting the researches in the field of shape memory composites. O.R. thanks the FRS-FNRS for a fellowship in the frame of a FRIA grant.

Conflict of Interest

The authors declare no conflict of interest.

Data Availability Statement

The data that support the findings of this study are available in the supplementary material of this article.

Keywords

electrospun mats, self-folding sheets, shape memory elastomer composites, surface topographies

Received: April 26, 2022
Revised: May 23, 2022
Published online:

[1] T. Cheng, M. Thielen, S. Poppinga, Y. Tahouni, D. Wood, T. Steinberg, A. Menges, T. Speck, *Adv. Sci.* **2021**, *8*, 2100411.
[2] E. Reyssat, L. Mahadevan, *J. R. Soc., Interface* **2009**, *6*, 951.
[3] L. Guiducci, J. W. C. Dunlop, P. Fratzl, *On Folding: Towards a New Field of Interdisciplinary Research*, Transcript, Verlag **2016**.
[4] G. Stoychev, S. Turcaud, J. W. C. Dunlop, L. Ionov, *Adv. Funct. Mater.* **2013**, *23*, 2295.
[5] Y. Cheng, K. Ren, C. Huang, J. Wie, *Sens. Actuators, B* **2019**, *298*, 126908.
[6] L.i Wang, Y. Jian, X. Le, W. Lu, C. Ma, J. Zhang, Y. Huang, C.-F. Huang, T. Chen, T. Chen, *Chem. Commun.* **2018**, *54*, 1229.
[7] Z. J. Wang, C. N. Zhu, W. Hong, Z. L. Wu, S. Zhen, *J. Mater. Chem. B* **2016**, *4*, 7075.
[8] X. Li, X. Cai, Y. Gao, M. J. Serpe, *J. Mater. Chem. B* **2017**, *5*, 2804.
[9] X. Wang, L. Li, E. Liu, J. Wang, X. Han, Y. Cao, C. Lu, *ACS Appl. Nano Mater.* **2021**, *4*, 5349.
[10] J. Kim, J. A. Hanna, M. Byun, C. D. Santangelo, R. C. Hayward, *Science* **2012**, *335*, 1201.
[11] X. Kuang, J. Wu, K. Chen, Z. Zhao, Z. Ding, F. Hu, D. Fang, H. J. Qi, *Sci. Adv.* **2019**, *5*, 5790.
[12] J. Odent, S. Vanderstappen, A. Toncheva, E. Pichon, T. J. Wallin, K. Wang, R. F. Shepherd, P. Dubois, J.-M. Raquez, J.-M. Raquez, *J. Mater. Chem. A* **2019**, *7*, 15395.
[13] G. Stoychev, S. Zakharchenko, S. Turcaud, J. W. C. Dunlop, L. Ionov, *ACS Nano* **2012**, *6*, 3925.
[14] C. E. Wisinger, L. A. Maynard, J. R. Barone, *Soft Matter* **2019**, *15*, 4541.
[15] A. Basu, J. Wong, B. Cao, N. Boechler, A. J. Boydston, A. Nelson, *ACS Appl. Mater. Interfaces* **2021**, *13*, 19263.
[16] Y. Mao, K. Yu, M. S. Isakov, J. Wu, M. L. Dunn, H. J. Qi, *Sci. Rep.* **2015**, *5*, 13616.
[17] J. Zhao, Q. Yang, T. Wang, L. Wang, J. You, Y. Li, Y. Li, *ACS Appl. Mater. Interfaces* **2017**, *9*, 43415.
[18] Y. Liu, J. K. Boyles, J. Genzer, M. D. Dickey, *Soft Matter* **2012**, *8*, 1764.
[19] Y. Liu, B. Shaw, M. D. Dickey, J. Genzer, *Sci. Adv.* **2017**, *3*, 1602417.
[20] J. Wong, A. Basu, M. Wende, N. Boechler, A. Nelson, A. Nelson, *ACS Appl. Polym. Mater.* **2020**, *2*, 2504.
[21] V. Lutz-Bueno, S. Bolisetty, P. Azzari, S. Handschin, R. Mezzenga, *Adv. Mater.* **2020**, *32*, 2004941.
[22] C. Yuan, T. Wang, M. L. Dunn, H. J. Qi, *Int. J. Precis. Eng. Man.* **2017**, *4*, 281.
[23] J. M. Robertson, A. H. Torbati, E. D. Rodriguez, Y. Mao, R. M. Baker, H. J. Qi, P. T. Mather, *Soft Matter* **2015**, *11*, 5754.
[24] Y. Mao, J. M. Robertson, X. Mu, P. T. Mather, H. J. Qi, *J. Mech. Phys. Solids* **2015**, *85*, 219.
[25] X. Wang, B. Ding, B. Li, *Mater. Today* **2013**, *16*, 229.
[26] A. Ranjan, T. J. Webster, *Nanotechnology* **2009**, *20*, 305102.
[27] N. Bink, V. B. Mohan, S. Fakirov, *Int. J. Polym. Mater. Polym. Biomater.* **2021**, *70*, 54.
[28] X. Dong, X. Yuan, L. Wang, J. Liu, A. C. Midgley, Z. Wang, K. Wang, J. Liu, M. Zhu, D. Kong, *Biomaterials* **2018**, *181*, 1.
[29] X. Luo, P. T. Mather, *Macromolecules* **2009**, *42*, 7251.
[30] J. N. Reddy, *Theory and Analysis of Elastic Plates and Shells*, CRC Press, Boca Raton, FL **2006**.
[31] R. M. Jones, *Mechanics of Composite Materials*, CRC Press, Boca Raton, FL **1998**.
[32] L. Gibson, M. Ashby, *Cellular Solids: Structure and Properties*, Cambridge University Press, Cambridge **1997**.
[33] E. D. Rodriguez, D. C. Weed, P. T. Mather, *Macromol. Chem. Phys.* **2013**, *214*, 1247.
[34] L. Zhang, J. Zhao, J. Xu, J. Zhao, Y. Zhu, Y. Li, J. You, *ACS Appl. Mater. Interfaces* **2020**, *12*, 42314.
[35] T. Nishikawa, M. Nonomura, K. Arai, J. Hayashi, T. Sawadaishi, Y. Nishiura, M. Hara, M. Shimomura, *Langmuir* **2003**, *19*, 6193.
[36] J. You, H. Fu, W. Dong, L. Zhao, X. Cao, Y. Li, Y. Li, *ACS Appl. Mater. Interfaces* **2012**, *4*, 4825.
[37] M. Nagata, Y. Yamamoto, *J. Polym. Sci., Part A: Polym. Chem.* **2009**, *47*, 2422.
[38] A. Goins, A. R. Webb, J. B. Allen, *Mater. Sci. Eng., C* **2019**, *97*, 896.
[39] C. M. Yakacki, R. Shandas, C. Lanning, B. Rech, A. Eckstein, K. Gall, *Biomaterials* **2007**, *28*, 2255.
[40] M.-C. Chen, H.-W. Tsai, Y. Chang, W.-Y. Lai, F.-L. Mi, C.-T. Liu, H.-S. Wong, H-W. Sung, *Biomacromolecules* **2007**, *8*, 2774.
[41] F. Gentile, L. Tirinato, E. Battista, F. Causa, C. Liberale, E. M. di Fabrizio, P. Decuzzi, *Biomaterials* **2010**, *31*, 7205.
[42] J. Zeng, M. Matsusaki, *Anal. Sci.* **2021**, *37*, 491.
[43] B. Gupta, A. Geeta, R. Ray, *J. Appl. Polym. Sci.* **2011**, *123*, 1944.

